

# IFU spectroscopy of Southern Planetary Nebulae IV: A Physical Model for IC 418

M.A. Dopita,<sup>1</sup> A. Ali,<sup>2,3</sup> R.S. Sutherland,<sup>1</sup> D.C. Nicholls,<sup>1</sup> & M. A. Amer,<sup>2,3</sup>

<sup>1</sup>Research School of Astronomy and Astrophysics, Australian National University, Cotter Rd., Weston ACT 2611, Australia

<sup>2</sup>Astronomy Dept, Faculty of Science, King Abdulaziz University, Jeddah, Saudi Arabia

<sup>3</sup>Department of Astronomy, Faculty of Science, Cairo University, Egypt

Released 2016 Xxxxx XX

## ABSTRACT

We describe high spectral resolution, high dynamic range integral field spectroscopy of IC418 covering the spectral range 3300–8950Å and compare with earlier data. We determine line fluxes, derive chemical abundances, provide a spectrum of the central star, and determine the shape of the nebular continuum. Using photoionisation models, we derive the reddening function from the nebular continuum and recombination lines. The nebula has a very high inner ionisation parameter. Consequently, radiation pressure dominates the gas pressure and dust absorbs a large fraction of ionising photons. Radiation pressure induces increasing density with radius. From a photoionisation analysis we derive central star parameters;  $\log T_{eff} = 4.525$ K,  $\log L_*/L_\odot = 4.029$ ,  $\log g = 3.5$  and using stellar evolutionary models we estimate an initial mass of  $2.5 < M/M_\odot < 3.0$ . The inner filamentary shell is shocked by the rapidly increasing stellar wind ram pressure, and we model this as an externally photoionised shock. In addition, a shock is driven into the pre-existing Asymptotic Giant Branch stellar wind by the strong D-Type ionisation front developed at the outer boundary of the nebula. From the dynamics of the inner mass-loss bubble, and from stellar evolutionary models we infer that the nebula became ionised in the last 100 – 200 yr, but evolved structurally during the  $\sim 2000$  yr since the central star evolved off the AGB. The estimated current mass loss rate ( $\dot{M} = 3.8 \times 10^{-8} M_\odot \text{yr}^{-1}$ ) and terminal velocity ( $v_\infty \sim 450$  km/s) is sufficient to excite the inner mass-loss bubble. While on the AGB, the central star lost mass at  $\dot{M} = 2.1 \times 10^{-5} M_\odot \text{yr}^{-1}$  with outflow velocity  $\sim 14$  km/s.

**Key words:** line: identification – shock waves – stars: post AGB – ISM: abundances – planetary nebulae: individual: IC418

## 1 INTRODUCTION

Reviewing the literature as listed in the SIMBAD database, we find that a daunting number of articles ( $\sim 950$ ) have studied the compact, young, high surface brightness, and low excitation class planetary nebula (PN) IC 418. These cover the entire accessible electromagnetic spectrum. Indeed, at first glance, it is difficult to imagine what can be contributed to the discussion on that object that is new.

The narrow band HST emission line images of this so-called “Spirograph nebula” show a well-defined oval shape with a simple radial ionization stratification and quasi-regular delicate filamentation. The HST color composite image ( $H\alpha + [O \text{ III}]$ ) displays a clearly enhanced filamentary  $[O \text{ III}]$  shell emission in the inner bubble region (Sahai et al. 2011). These authors suggested that this inner bubble represents emission from very hot gas in the reverse shock generated by the spherical, radiatively driven, fast wind from

the central star (CS). Here we present a somewhat different model. To investigate the occurrence of shocks in planetary nebulae (PNe), Guerrero et al. (2013) have built  $[O \text{ III}]/H\alpha$  ratio maps which show a decrease at the outer edge in case of IC 418. The optical, near, and mid-IR images probe the presence of different structures around the bright main nebular shell including radial filaments/rays, a system of three concentric rings and two detached haloes (Ramos-Larios et al. 2012). Some of these features can be ascribed to enhanced mass-loss during thermal pulses occurring at the end of the AGB phase of stellar evolution (Vassiliadis & Wood 1993). Furthermore, they noticed that the progression of the ionization front through the nebula is not homogenous, with the development of instabilities at the outer regions of the ionized shell (which give rise to the “spirograph” appearance), and the formation of radial structures probably caused by UV photons leaking from the less opaque regions of the ionised shell.

The central star (CS) of IC 418 (HD 35914) has been classified as an Of (H-rich) type (Acker et al. 1992). It has a relatively a low temperature as determined from the Zanstra ( $T_Z(\text{H I}) = 34\text{kK}$ ) and energy balance ( $T_{\text{EB}} = 36\text{kK}$ ) methods (Pottasch & Bernard-Salas 2010). Due to the marginally detected He II  $\lambda 4686$  emission of IC 418, which (as shown here) seems to originate mainly in the central star, it is hard to derive a realistic He II Zanstra temperature. Presumably, it was this central star HeII emission which led Phillips (2003) to derive the much higher He II Zanstra temperature ( $T_Z(\text{He II}) = 44.5\text{kK}$ ).

Evidence for a hot shocked stellar wind and possible electron conduction region in the inner region of IC 418 has been found by Ruiz et al. (2013) (see the Chandra and HST color composite image of IC 418 in their Figure 3). These authors find diffuse X-rays in a number of nebulae showing O VI nebular emission in the UV. In the specific case of IC 418, the *Chandra* data is consistent with thermal emission from a hot plasma confined within the inner [O III] bright filamentary shell at a temperature of  $0.26\text{keV}$  ( $3 \times 10^6\text{K}$ ).

Time-variability structure in the fast winds of the IC 418 CS was detected by Prinja et al. (2012). They reported that the UV resonance line in the IC 418 CS are variable primarily due to the occurrence of blue-ward migrating discrete absorption components. Polarimetric spectra of the CS indicate mean longitudinal magnetic fields of  $\sim 200\text{G}$  (Steffen et al. 2014).

Among recent significant works we note the superb échelle spectrum by Sharpee et al. (2003, 2004), which provided accurate line identifications and fluxes over a wide wavelength base, and down to very faint levels. This work enables a comparison of line fluxes with those from our own IFU observations and with those derived from the model which we present in this paper. Both the Sharpee et al. (2003) work and the UV and IR spectrophotometry published by Pottasch et al. (2004) were used by Morisset & Georgiev (2009) to construct a self-consistent stellar and 3D nebular model for IC418 which reproduces the optical and UV stellar observations as well as the nebular IR, deep optical, UV observations, and HST images. The model provides an effective temperature,  $T_{\text{eff}} = 36.7 \pm 0.5\text{kK}$  and a luminosity of  $7700 L_{\odot}$  for the CS. Further, the model shows that the abundances of O, Ne, and Ar elements are close to solar values, while the elements Si, S, Cl, Mg, and Fe are under-abundant relative to their solar values, indicating trapping of an appreciable fraction of these elements on to dust grains. This work was expanded later by Escalante et al. (2012) to show that many of the faint permitted lines of the heavy elements are predominantly excited by fluorescence rather than by recombination.

Delgado-Inglada et al. (2015) have classified IC 418 as a carbon-rich dust PN due to the presence of the infrared broad features at  $11$  and/or  $30\ \mu\text{m}$  associated with SiC and MgS. From the comparison of He/H, C/O, and N/O abundance ratios derived from the PNe with predictions of nucleosynthesis models, they suggest that PNe with carbon-rich dust descend from stars with masses in the range  $1.5$ - $3.0$  solar masses. Otsuka et al. (2014) confirmed the presence of the broad PAH  $3.3\ \mu\text{m}$  emission band and measured the total flux of the  $17.4$  and  $18.9\ \mu\text{m}$  emission F( $\text{C}_{60}$  - fullerenes) and its fraction with respect to the integrated dust continuum. Díaz-Luis et al. (2015) identified 11 diffuse interstellar bands

in IC 418, but they found no evidence for the strongest electronic transition of neutral  $\text{C}_{60}$ . The first detection of the isotope  $^3\text{He}$  in IC 418 was reported by Guzman-Ramirez et al. (2016). They derived abundance in the range  $1.7 \pm 0.8 \times 10^{-3}$  to  $3.8 \pm 1.7 \times 10^{-3}$  for  $^3\text{He}/\text{H}$ . Such a discovery clearly has impact in the fields of astrophysics and cosmology.

The integral field unit (IFU) technique (as applied to PNe) was pioneered by Monreal-Ibero et al. (2005) and Tsamis et al. (2007). Recently, detailed physical and morpho-kinematical studies using optical IFU data have been obtained by Danehkar & Parker (2015), Danehkar (2015) and Danehkar et al. (2016) using the Wide Field Spectrograph (WiFeS) instrument (Dopita et al. 2007, 2010) to study the PNe Hen 3-1333, Hen 2-113, Th 2-A and M2-42. The advantages of using the integral field unit (IFU) spectroscopy compared to the long slit spectroscopic technique in the field of planetary nebulae, were given by Ali et al. (2016). This paper is the fourth in the series examining PNe using the unique capabilities of the WiFeS instrument, which is uniquely well-suited to integral field spectroscopy of compact PNe. In the first paper in this series, Ali et al. (2015) used WiFeS to study the large, evolved and interacting planetary nebula PNG 342.0-01.7, generating an IFU mosaic to cover the full spatial extent of the object. The second paper, (Basurah et al. 2016) provided a detailed analysis of four highly excited non-type I PNe which casts doubt on the general applicability of the WELS classification. The third paper (Ali et al. 2016) presented excitation maps, integral field spectroscopy and an abundance analysis of the four PNe: M3-4; M3-6; Hen2-29; Hen2-37. In addition we demonstrated that the CS of M3-6 is another example for the mis-classified WELS group of nebulae.

These earlier papers used a resolution of  $R = 7000$  in the red out to  $7200\text{\AA}$  and a resolution of  $R = 3000$  in the blue region of the spectrum ( $\sim 3600 - 5600\text{\AA}$ ). In this paper we provide emission line modelling of integral field data covering whole nebula over the full wavelength range of the WiFeS instrument ( $3300-8950\text{\AA}$ ), and at the highest resolution available ( $R = 7000$ ). This modelling includes both the effect of the inner [O III] - bright shock, driven into the ionised plasma by the overpressure of the hot shocked stellar wind bubble, and the shock at the outer boundary of the ionised region propagating into the AGB wind, which must be driven by the strong D-type ionisation front formed as both the effective temperature and number of ionising photons produced by the central star rapidly increase with time (Kahn 1954; Mendis 1969; Garcia-Segura & Franco 1996).

In Section 2, we describe the observations and data reduction, while the nebular and stellar spectra in addition to reddening corrections are discussed in Section 3. The basic parameters of the three zones in a self-consistent model of IC 418, and the details of the model are given in Sections 4 and 5, respectively. Section 6, is dedicated to the results of the nebular model, while Section 7 provides the discussion and conclusions.

## 2 OBSERVATIONS & DATA REDUCTION

The integral field spectra of IC 418 were obtained on January 9, 2016 using the WiFeS instrument (Dopita et al. 2007, 2010) mounted on the 2.3-m ANU telescope at Siding Spring

**Table 1.** The log of WiFeS observations of IC 418

Gratings	No. of frames	PA (deg)	Exposure time (s)	Date	Standard & Telluric Stars
<b>IC 418:</b>					
U7000 & R7000	3	90	3	09/01/2016	HD 009051, HD 074000 & HIP 14898 (telluric)
U7000 & R7000	3	90	10	09/01/2016	"
U7000 & R7000	3	90	30	09/01/2016	"
U7000 & R7000	3	90	100	09/01/2016	"
<b>Sky Reference:</b>					
U7000 & R7000	3	0	300	09/01/2016	"
<b>IC 418:</b>					
B7000 & I7000	6	90	3	09/01/2016	HD 009051, HD 074000 & HIP 14898 (telluric)
B7000 & I7000	3	90	10	09/01/2016	"
B7000 & I7000	3	90	30	09/01/2016	"
B7000 & I7000	3	90	100	09/01/2016	"
<b>Sky Reference:</b>					
B7000 & I7000	3	0	300	09/01/2016	"

Observatory. This instrument delivers a field of view of  $25'' \times 38''$  at a spatial resolution of either  $1.0'' \times 0.5''$  or  $1.0'' \times 1.0''$ , depending on the binning on the CCD. In these observations, we operated in the binned  $1.0'' \times 1.0''$  mode. The data were obtained in the high resolution mode  $R \sim 7000$  (FWHM of  $\sim 45$  km/s) using all four high-resolution gratings. Observations are made simultaneously in two gratings, as indicated in Table 1. For the U7000 & R7000 gratings, the dichroic cuts at 480nm (RT480), while for the B7000 & I7000 gratings, the dichroic cuts at 615nm (RT615). Thus each waveband is observed in a region of high dichroic efficiency, and an adequate overlap in wavelength coverage is obtained between each of the gratings. For details on this, see Dopita et al. (2007).

The wavelength scale was calibrated using the Ne-Ar arc lamp throughout the night. Arc exposure times are 180s for the U7000 grating, 100s at B7000, 9s for the R7000, and 1s for the I7000 grating. Flux calibration was performed using the STIS spectrophotometric standard stars HD 009051 & HD 074000<sup>1</sup>. In addition, a B-type telluric standard HIP 14898 was observed to better correct for the OH and H<sub>2</sub>O telluric absorption features in the red. The separation of these features by molecular species allows for a more accurate telluric correction by accounting for night to night variations in the column density of these two species. All data cubes were reduced using the PyWiFeS<sup>2</sup> data reduction pipeline (Childress et al. (2014)). A summary of the spectroscopic observations is given in Table 1.

The global spectra of each of the objects were extracted from their respective reduced data cubes using a circular aperture matching the observed extent of the PNe using QFitsView v3.1 rev.741<sup>3</sup>. This procedure allows for sub-arcsec. differences in the extraction apertures caused by differential atmospheric dispersion. All spectra are sky subtracted using the sky reference exposures listed in Table 1. In the I7000 and R7000 wavebands, any residual night sky

lines were removed using an annular region outside the observed extent of the PNe.

Except in the shortest exposures, the strong lines are saturated on the CCD. Even in the shortest exposure the [O III]  $\lambda 5007\text{\AA}$  line is marginally saturated, and for this line the flux was determined from the [O III]  $\lambda 4959\text{\AA}$  line, multiplied by its theoretical ratio with respect to [O III]  $\lambda 5007\text{\AA}$   $R(5007/4959) = 2.89039$ .

The continuum levels and the faint emission lines are determined from the longest exposures in each grating. For the stronger lines, saturation on the CCD is detected by comparison of the measured peak flux between two exposures. If the measured peak flux in the longer exposure is lower, then the line is saturated. The data in the saturated region was then replaced by the unsaturated data in the corresponding region.

Finally emission-line fluxes, their uncertainties, the velocity FWHMs and the continuum levels were measured, from the final combined, flux-calibrated spectra, using the interactive routines in Graf<sup>4</sup> and in Lines<sup>5</sup>. Each line is fit with a single Gaussian, which at this resolution provides a sufficient description of the line profile. The local continuum is fit either side of the line using a linear or a quadratic interpolation. The measured wavelength, the wavelength corrected to rest, and the NIST wavelength of all the identified lines are listed in Table ?? in the Appendix. The mean wavelength error on the identification can be estimated for each grating as a function of wavelength from Fig 1. The identification of the lines in common with this study can be made by comparing Table ?? with Table 3 of Sharpee et al. (2003).

## 3 RESULTS

### 3.1 Nebular and Stellar Spectra

In Figure 2 we show the extracted spectra of the IC 418 nebula, and of its central star, and in Figure 3 we show the

<sup>1</sup> Available at :

[www.mso.anu.edu.au/~bessell/FTP/Bohlin2013/G012813.html](http://www.mso.anu.edu.au/~bessell/FTP/Bohlin2013/G012813.html)

<sup>2</sup> <http://www.mso.anu.edu.au/pywifes/doku.php>.

<sup>3</sup> QFitsView v3.1 is a FITS file viewer using the QT widget library and was developed at the Max Planck Institute for Extraterrestrial Physics by Thomas Ott.

<sup>4</sup> Graf is written by R. S. Sutherland and is available at: <https://miocene.anu.edu.au/graf>

<sup>5</sup> Lines is written by R. S. Sutherland and is available at: <https://miocene.anu.edu.au/lines>

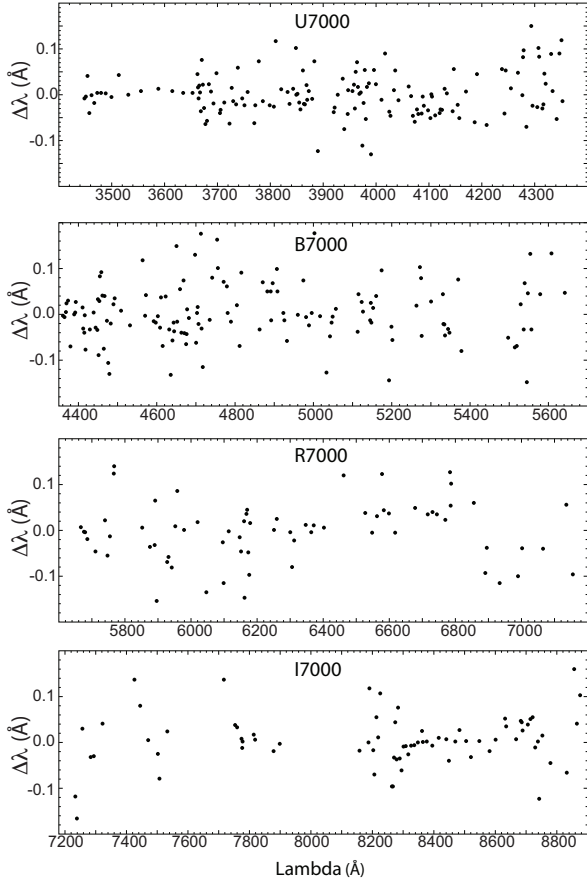


**Figure 1.** The difference between the measured rest wavelength for emission lines in IC 418 and the NIST wavelength of the line identification as a function of both wavelength and grating used. The typical RMS error is  $\pm 0.05\text{\AA}$ .

nebular spectrum in the spectral region  $4240\text{--}4840\text{\AA}$  amplified to bring out the fainter lines and to show the noise in the continuum determination. A number of O II and N II recombination lines are marked. The signal to noise in the nebular continuum is better than 100:1, except in regions of strong residual telluric absorption. These regions show up clearly in the spectrum of the central star. Nonetheless, the quality of the telluric correction is very high, as these residual features only amount to a few percent. Table ?? in the Appendix lists the measured line fluxes with respect to  $H\beta = 100$ , the estimated flux error and the reddening corrected fluxes (see below for the derivation of these). We also measured line FWHM in velocity, without correction for the instrumental profile ( $V_{FWHM} = 45 \pm 5 \text{ km/s}$ ).

The observed  $H\beta$  flux for the full ionised nebula is  $\log F_{H\beta} = -9.54 \pm 0.01$ , in agreement with Pottasch et al. (1977). Previously published values range from  $-9.52$  to  $-9.71$  (Capriotti & Daub 1960; O’Dell 1962; Perek 1971; Kaler 1973; Carrasco et al. 1983). Using a logarithmic reddening correction of  $c = 0.26$  based on the ratio of  $H\alpha$  to  $H\beta$ , we deduce a reddening corrected flux of  $\log(F_{H\beta}) = -9.28 \pm 0.01$ .

### 3.2 Reddening Corrections

The standard way to infer the reddening correction is from measurement of the Balmer Decrement. On this basis we infer a logarithmic reddening correction of  $c = 0.26$  for IC 418. This is very similar to the extinction inferred from the  $\lambda 2200\text{\AA}$  dip by Pottasch et al. (1977);  $c = 0.28$ . However, given the high quality spectrophotometric data presented here, we can also use Balmer to Paschen ratios, the recombination lines of He I, and/or the shape of the nebular continuum, (Groves et al. 2002). However, to do this, we first need a nebular model against which we can compare our observations. The details of the final model are given below. However, for the purpose of deriving the reddening, we first produced an approximate model to fit the observed line intensities using our estimated logarithmic reddening correction of  $c = 0.26$ . We then inferred an empirical reddening function on the basis of the model line intensities compared with the observations, and using the model nebular continuum compared with the observations. We then used the revised line intensities to obtain an improved model, and repeated the process. Two iterations are sufficient for the process to converge satisfactorily.

The resultant differential reddening function is shown in Figure 4. The continuum and the He I lines agree well, as does the Balmer decrement for the well-separated lines. However, the closely spaced Balmer and Paschen lines systematically deviate from the smooth reddening function. A comparison with the Sharpee et al. (2003) line intensities suggests that these overlapping lines are not well measured in our line fitting procedure, and should be discounted from the fit.

The derived de-reddened line fluxes are presented in Table ?? in the Appendix. A total of 636 emission lines have been identified.

### 3.3 Basic Temperature and Density Diagnostics

We have used the emission line fluxes measured from the global nebular spectrum, and listed in Table ?? in the Appendix to determine electron temperatures, densities and ionic abundances using the Nebular Empirical Abundance Tool (NEAT; Wesson et al. (2012) to derive the electron temperature and density from the low and medium-ionization zones. The NEAT code use the Monte Carlo technique to propagate the statistical uncertainties from the line fluxes to the temperature, density, ionic, and elemental abundances. The NEAT temperatures and electron densities are given in Table 2, where we also include the values derived from our detailed photoionisation modelling described below as well as those previously derived in the literature.

In Table 3 we provide the derived elemental abundances from this work, and from the literature. Note that the optical recombination lines (ORLs) of both N and O give a much larger abundance than the collisionally excited lines (CELs). This difference has been shown by Escalante et al. (2012) to be mainly caused by fluorescent effects caused by the UV continuum of the central star, and is discussed in detail in Section 6.3 below.

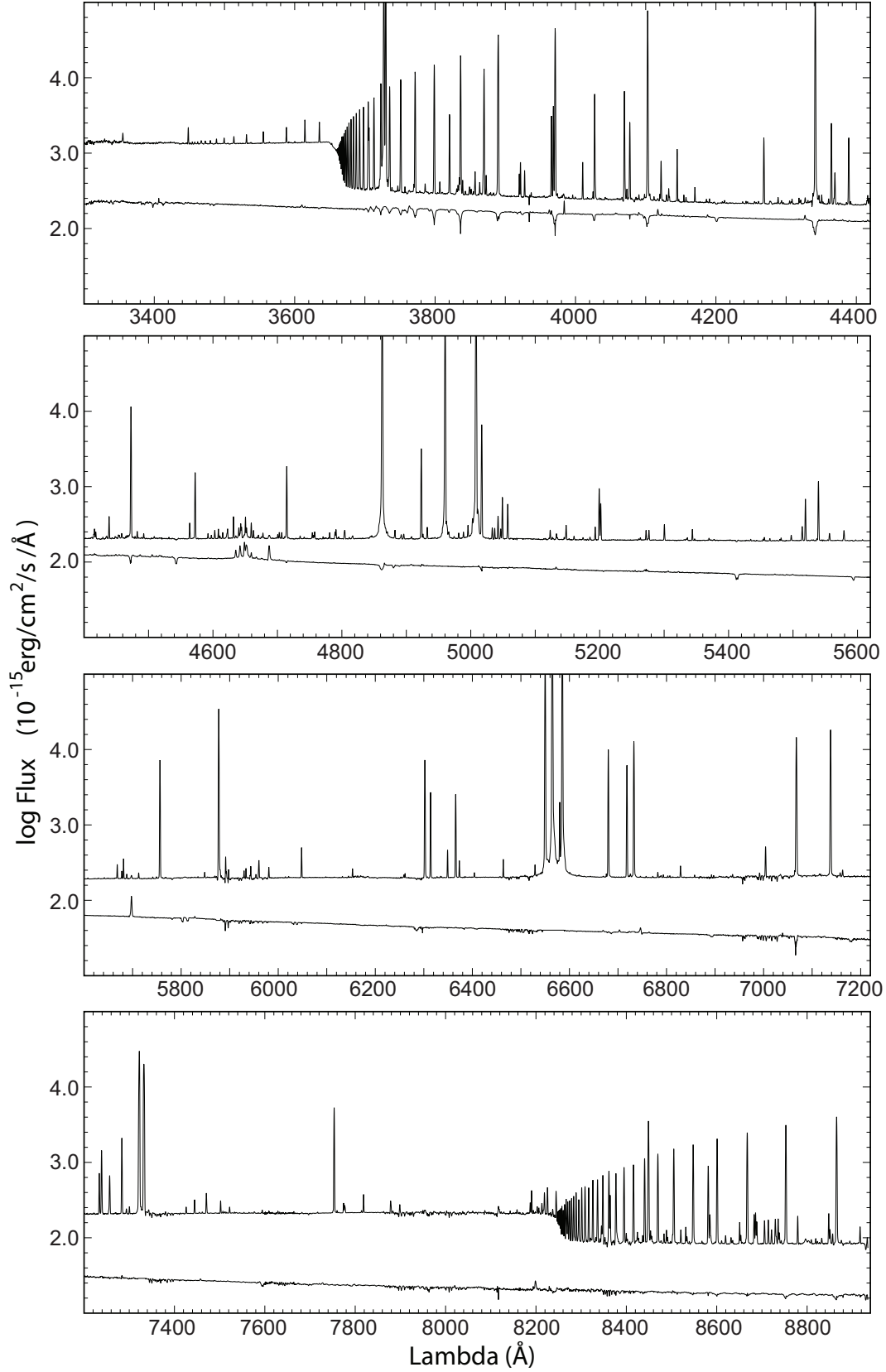


**Figure 2.** The WiFeS spectrum of the IC 418 nebula (upper curves) and of its central star (lower curves). To bring out fainter lines, the flux scale is logarithmic. For the star, the H $\gamma$  to H $\alpha$  absorption profiles are likely to be in error because of saturation effects. Note the NIII/CHII/C IV emission line complex in the central star at 4630–4660Å and the broad He I and H I line absorption lines. The diffuse interstellar absorption bands presented in the high-dispersion spectra by [Díaz-Luis et al. \(2015\)](#) at 5780, 5797Å are also visible here.

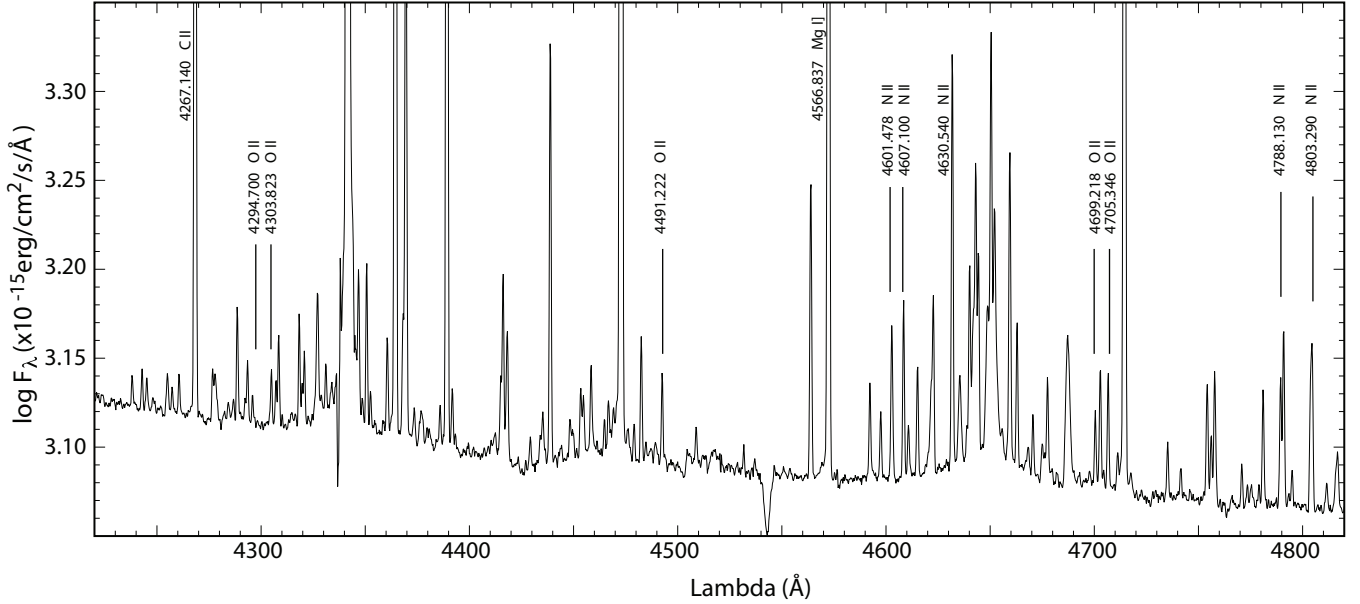


**Figure 3.** The WiFeS spectrum of the IC 418 nebula enlarged to show a region with O II, NII and CII recombination lines. A few of these are identified on the figure. Note that the noise on the continuum is only  $\sim \pm 0.02$  dex, and that crowding of faint lines can become a problem for their accurate measurement at this resolution.

**Table 2.** Average electron temperatures and densities of IC 418 derived from the IFU spectrum compared with those given in the literature, and by the self-consistent photoionisation model described below.

Object	Temperature (K)					Density ( $\text{cm}^{-3}$ )		
	$T_{[\text{OIII}]}$	$T_{[\text{NII}]}$	$T_{[\text{SII}]}$	$T_{[\text{ArIII}]}$	$T_{[\text{OII}]}$	$n_{[\text{SII}]}$	$n_{[\text{OII}]}$	$n_{[\text{CIII}]}$
<b>IC 418</b>								
Observed:	$8775^{+75}_{-75}$	$10008^{+420}_{-420}$	$9879^{+4941}_{-4878}$	$8489^{+108}_{-108}$	$9216^{+150}_{-190}$	$8374^{+5024}_{-6382}$	$11874^{+8078}_{-3688}$	$11178^{+679}_{-679}$
Model:	8800	8830	8680	8879	8856	11950	12120	11450
Ref (1)	$8780^{+150}_{-190}$	$9530^{+390}_{-370}$		9100		$15300^{+16000}_{-6600}$	$9000^{+4800}_{-2300}$	$10400^{+1700}_{-1800}$
Ref (2)	$8900^{+400}_{-400}$	$9400^{+900}_{-1400}$	$7000^{+4000}_{\dots}$	$9000^{+500}_{-400}$	$10000^{+4000}_{-3000}$	$17000^{+9000}_{\dots}$	$10000^{+17000}_{-5000}$	$11000^{+4000}_{-2000}$
Ref (3)	9100	9400		9100		3100	5000	4300

References: (1) [Delgado-Inglada et al. \(2015\)](#); (2) [Sharpee et al. \(2004\)](#); (3) [Pottasch et al. \(2004\)](#)

#### 4 A PHYSICAL MODEL FOR IC418

We aim to construct a self-consistent model for IC 418 consisting of three separate zones:

- (i) An inner photoionised shock driven by the accelerating stellar wind of the central star,
- (ii) A photoionised nebular shell, and
- (iii) An outer shock in the AGB wind driven by the over-pressure of the strong D-Type ionisation front.

Here, we estimate the basic parameters of these three zones.

##### 4.1 The inner stellar wind bubble shock

The inner photoionised shocked shell is expected to exist from the theory of mass-loss bubbles ([Dyson & de Vries 1972](#); [Weaver et al. 1977](#); [Schmidt-Voigt & Koeppen 1987](#);

[Schmidt-Voigt & Koppen 1987](#); [Marten & Schoenberner 1991](#)) and is clearly visible in the HST *Hubble Heritage* image (<http://heritage.stsci.edu/2000/28/big.html>) as an elliptical filamentary ring, enhanced in [O III] emission. This ring, approximately 0.01 pc in diameter, is coincident with the extent of the diffuse X-ray emission seen with *Chandra* ([Ruiz et al. 2013](#)). The X-ray emission arises from a thermal plasma at  $T_e \sim 3 \times 10^6$  K. This temperature would be produced by a shocked stellar wind from the central star, provided that the terminal velocity of this wind is  $v_w \sim 500$  km/s – or somewhat faster if cooling of the hot plasma by thermal conduction is important. This compares with the value of  $v_w$  estimated from the UV observations of the central star by [Morisset & Georgiev \(2009\)](#); 450 km/s.

The pressure driving the outer stellar wind shock can be estimated from the properties of the stellar wind itself. From [Morisset & Georgiev \(2009\)](#), the stellar mass-loss rate

**Table 3.** Observed abundances by number with respect to H both derived from the NEAT code and compared with previous work.

Element	Abundances from NEAT		Abundances from literature	
	ORLs	CELs	Ref 1	Ref 2
He/H	$7.97E-2^{+1.9E-3}_{-1.9E-3}$	–	$9.1E-02^{+9.1E-4}_{-9.1E-4}$	$>7.20E-2$
C/H	$5.50E-4^{+1.1E-5}_{-1.1E-5}$	–	$6.17E-4^{+1.9E-4}_{-2.1E-4}$	$6.20E-4$
N/H	$3.10E-4^{+4.7E-6}_{-4.7E-6}$	$4.51E-5^{+3.4E-6}_{-4.5E-5}$	$6.61E-5^{+1.1E-5}_{-7.3E-6}$	$9.50E-5$
O/H	$9.97E-4^{+8.1E-4}_{-3.0E-4}$	$2.20E-4^{+6.6E-5}_{-2.2E-4}$	$3.47E-4^{+3.1E-5}_{-3.1E-5}$	$3.50E-4$
Ne/H	$7.32E-5^{+2.2E-5}_{-1.6E-5}$	$3.16E-5^{+8.6E-6}_{-4.0E-6}$	$3.47E-5^{+1.7E-6}_{-4.2E-6}$	$8.8E-5$
Ar/H	–	$1.72E-6^{+5.3E-7}_{-1.7E-6}$	$1.12E-6^{+1.6E-7}_{-3.5E-7}$	$1.80E-6$
S/H	–	$1.89E-6^{+2.1E-7}_{-1.1E-7}$	–	$4.4E-6$
Cl/H	–	$8.92E-8^{+3.1E-9}_{-2.9E-9}$	$8.7E-8^{+3.5E-9}_{-9.6E-9}$	–
N/O	0.31	0.21	0.19	0.27

References: (1) Delgado-Inglada et al. (2015); (2) Pottasch et al. (2004)

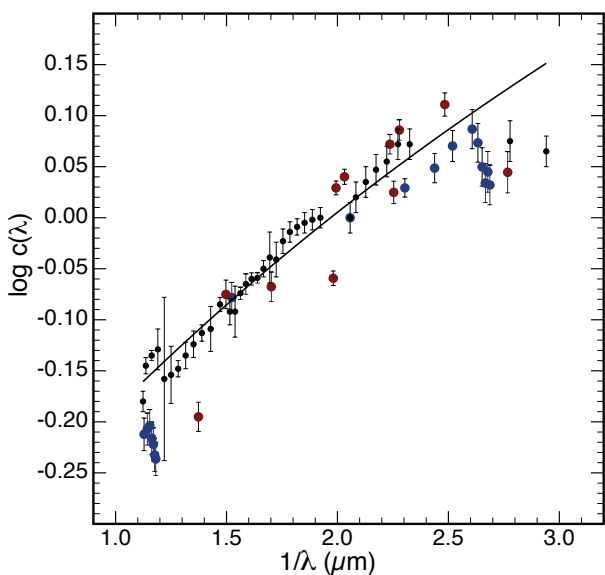


**Figure 4.** The inferred differential reddening function in IC 418. The black points are values inferred from the nebular continuum, the blue points are obtained for the Balmer and Paschen lines of Hydrogen while the red points refer to the He I recombination lines. The black line is the adopted fit to the data.

$\dot{M} = 3.8 \times 10^{-8} M_{\odot} \text{yr}^{-1}$ . The momentum flux in the stellar wind is converted to thermal pressure at the edge of the free-wind region, which theoretical models indicate lies between 0.5–0.7 of the radius of the shock in the swept up AGB wind. At a distance of 1.0 kpc, derived below, this [O III] - bright stellar wind shock lies at a radius of  $\sim 0.01$  pc. Using a stellar wind velocity of  $v_w \sim 500$  km/s, we find that both the hot X-ray bubble and the shocked [O III] bubble has  $\log P/k = 8.2 - 8.5 \text{ cm}^{-3} \text{K}$ . We will use this estimate later

to compute the velocity of the stellar wind bubble shock in the photoionised nebula.

## 4.2 The photoionised nebula

A self-consistent model of the photoionised region of IC 418 has been presented by Morisset & Georgiev (2009). In order to reproduce the surface brightness distribution, a particular density distribution was imposed for both the inner photoionised stellar wind shock and for the photoionised nebula as a whole. However, this distribution may be a natural consequence of the somewhat unusual parameters of the nebula. Based on an inner radius of 0.01 pc, and depending upon the density at this inner radius, we estimate that the ionisation parameter at the inner boundary of the photoionised nebula is in the range  $-0.1 > \log \mathcal{U} > -0.5$ . This puts IC 418 very firmly into the category of nebulae in which radiation pressure exceeds the gas pressure (Dopita et al. 2002, 2006; Davies et al. 2016). In this regime, dust competes very successfully with the ionised plasma to absorb photons in the Lyman continuum, reducing the extent of the photoionised nebula (Dopita et al. 2003), while at the same time, radiation pressure induces a steeply increasing density gradient through the photoionised nebula, as the radiation field is absorbed and its pressure adds to the initial gas pressure. Such a density gradient is observed in IC 418, and our modelling seeks to discover whether this is simply due to the action of radiation pressure.

## 4.3 The outer shock in the AGB wind

As a consequence of the pressure in the photoionised region, which includes both the gas pressure, and the pressure associated with the absorbed fraction of the radiation field at the outer ionised boundary, a strong D-type ionisation front is formed (Kahn 1954; Mendis 1969; Garcia-Segura & Franco 1996). The structure of this is as follows. Immediately beyond the photoionised region, lies a strongly compressed un-ionised shell. The pressure in this shell matches the sum of

the gas pressure and radiation pressure in the ionised region, plus the pressure associated with the recoil momentum of the newly-ionised gas flowing into the photoionised region. Because this un-ionised shell has a much higher pressure than the surrounding undisturbed AGB wind, an expanding shock (assumed isothermal) is located at its outer boundary, such that the ram pressure of the AGB wind being swept up by the shock is equal to the internal pressure of the shell.

The dense shell of un-ionised gas around the strong D-Type ionisation front is Rayleigh-Taylor unstable (Frieman 1954; Spitzer 1954). However, even if the shell is accelerating, these instabilities can be stabilised by recombination (Kahn 1958; Axford 1964; Williams 1999), and in this case, the ionisation front may oscillate about its mean instantaneous radius with time (Mizuta et al. 2005). A full 3-D treatment for the specific case of an ionisation front propagating into a  $r^{-2}$  density distribution (which is particularly applicable to PNe) has been made by Whalen & Norman (2008). This work shows that fine perturbations or crinkles in the D-Type ionisation front grow, merge and ultimately break out to form “elephant trunks” along with isolated neutral inclusions remaining from the dense shell. It would appear that the “spirograph” appearance of the outermost parts of IC 418 are an early manifestation of this ionisation front instability.

The velocity of the outer shock in the AGB wind can be estimated by combining the angular expansion rate measured by Guzmán et al. (2009) with the HI absorption velocity determined by Taylor & Pottasch (1987). Adopting a distance of  $1.0 \pm 0.1$  kpc derived from the model presented below, and the angular expansion rate of the ionization front in IC 418 from Guzmán et al. (2009) ( $5.8 \pm 1.5$  mas/yr), gives a shell expansion velocity of 27.4 km/s. However, the H I absorption feature detected by Taylor & Pottasch (1987) is at  $-13.2$  km/s with respect to the systemic velocity. This implies that the outer shock has a velocity equal to the difference between these numbers;  $\sim 14$  km/s. This is strongly supersonic with respect to the cool AGB wind, and such a shock is still capable of producing some optical emission.

## 5 DETAILS OF THE MODEL

### 5.1 The Photoionised Nebula

To model IC 418, we have used the **Mappings V version 5.1.12** code (Sutherland et al. 2017, submitted)<sup>6</sup>. Earlier versions of this code have been used to construct photoionisation models of H II regions, PNe, Herbig-Haro Objects, supernova remnants and narrow-line regions excited by AGN. This code is the latest version of the **Mappings 4.0** code earlier described in (Dopita et al. 2013), and includes many upgrades to both the input atomic physics and the methods of solution.

We choose as the initial abundance set the local galactic concordance (LGC) abundances (Nicholls et al. 2017) based upon the Nieva & Przybilla (2012) data on local galactic main sequence B stars. This provides the abundances of the main coolants, H, He, C, N, O, Ne, Mg, Si and Fe and the ratios of N/O and C/O as a function of abundance. For the

light elements we use the Lodders et al. (2009) abundance, while for all other elements the abundances are based upon Scott et al. (2015a,b) and Grevesse et al. (2010). The individual elemental abundances are then iterated from this initial set in order to minimise the offset of the model with respect to the observations for all the lines of any given element.

In the modelling, dust physics is very important. Not only do dust grains remove coolants from the nebular gas, but they are also an important source of photoelectric heating (Dopita & Sutherland 2000). Furthermore, the pressure of the radiation field is primarily coupled to the dust absorption, and in objects such as IC 418, the effect of competition by dust grains with the gas for the absorption Lyman continuum photons is fierce. IC 418 shows a large depletion of the heavy elements onto dust, as evidenced by the depletion of Ca, Mg, and Fe (see below). This suggests the presence of silicates, since we have no physical mechanism to deplete these elements in the stellar envelope.

The detailed dust physics as currently implemented in the Mappings V code has been described in detail by Dopita et al. (2005). Briefly, this consists of PAHs (not included in the IC 418 model), amorphous carbon and silicate grains. For the latter two categories, we use 80 bins in the size distribution, usually taken as a standard Mathis et al. (1977) distribution. We allow for grain charging, photoelectron emission and grain temperature fluctuations in the computation of the IR emission. An improved version of this dust physics has been implemented by Morisset et al. (2012) for the specific case of IC 418, and these authors succeed in reproducing the IR spectrum of the dust thermal emission. As a consequence, we do not attempt to emulate this work here. For the initial depletion factors we use the Jenkins (2009) scheme, with a base depletion of Fe of 2.25 dex, but these are adjusted by individual element to best fit the observations. We obtain a final dust to gas mass ratio of  $1.12 \times 10^{-2}$ . The carbon rich nature of the nebula naturally gives rise to a carbon grain dominant dust composition in the models. The dust to gas mass ratio for the carbon grains alone is  $3.8 \times 10^{-3}$ . This should be compared to the value of  $\sim 6 \times 10^{-4}$  derived by Hoare (1990) and Meixner et al. (1996). It should be noted that these works provide a reasonable fit to the cool dust emission, but fail by a factor of 3 or so to explain the hot dust emission seen by Omont et al. (1995) which peaks at  $\sim 30 \mu\text{m}$ , and which is ascribed by these latter authors as possibly due to MgS.

For the central star, we follow Morisset & Georgiev (2009) in using the CMFGEN model atmospheres from Hillier & Miller (1998). Morisset & Georgiev (2009) used the detailed profiles of the hydrogen absorption lines to constrain the effective gravity of the star ( $\log g = 3.5$ ) and used the excitation of the nebula to constrain the effective temperature ( $T_{eff} = 36.7\text{kK}$ ). Here we have iterated the effective temperature to match the observed excitation of the nebula, once the density structure has been fixed to reproduce the density sensitive line ratios, with the exception of [Ar IV] which is produced in the inner photoionised shock produced by the stellar wind. We find  $T_{eff} = 33.5\text{kK}$ , somewhat lower than that obtained by Morisset & Georgiev (2009), probably because of the different nebular dust physics used here. As mentioned above, for this nebula the radiation pressure acting mainly on dust produces a strong positive radial density

<sup>6</sup> Available at <https://miocene.anu.edu.au/mappings>



gradient. In our models, at the inner radius of 0.01 pc., the ionisation parameter is  $\log U = -0.1$  and the gas pressure is  $\log P/k = 7.4$ . As the radiation field is absorbed in the ionised shell, the pressure rises to  $\log P/k = 8.4 \text{ cm}^{-3}\text{K}$ . As a result, the inner electron density is only  $n_e = 1550 \text{ cm}^{-3}$ , but it peaks at  $n_e = 27160 \text{ cm}^{-3}$ . This causes the steep increase in surface brightness empirically modelled by [Morisset & Georgiev \(2009\)](#). This is discussed further below.

Although the nebula is mildly elliptical (outer diameter  $10.7 \times 13.7$  arc sec. and inner diameter  $3.2 \times 4.3$  arc sec.), we model it as a spherical shell with filling factor unity. Our model aims to match both the observed mean diameter and the absolute  $H\beta$  flux at the assumed distance. Because of the competition of dust for the ionising photons, the method used by [Basurah et al. \(2016\)](#) to estimate the distance does not work. For a given luminosity of the central star, the computed absolute  $H\beta$  luminosity hardly changes with distance, because, for smaller assumed distances, the ionisation parameter at the inner radius of the shell rises, and the fraction of ionising photons absorbed by dust rises. However, a solution which matches both the observed mean diameter and the absolute  $H\beta$  flux can still be obtained. With this we find  $\log L_* = 4.029$  and a distance,  $D = 1.0 \pm 0.1$  kpc. At assumed distances of 0.9, 1.0 and 1.1 kpc, the corresponding computed absolute  $H\beta$  fluxes are  $\log L_{H\beta} = 34.76, 34.78$  and  $34.80$ . The observed absolute  $H\beta$  fluxes corrected for reddening and using these same assumed distances are  $\log L_{H\beta} = 34.69, 34.78$  and  $34.87$ , respectively.

In order to measure the goodness of fit of any particular photoionisation model, we measure the degree to which it reproduces the density-sensitive line ratios, and we also seek to minimise the L1-norm for the fit for the main coolant lines, and for the H and He recombination lines - for a total of 34 lines. That is to say that we measure the modulus of the mean logarithmic difference in flux (relative to  $H\beta$ ) between the model and the observations *viz.*;

$$L1 = \frac{1}{m} \sum_{n=1}^m \left| \log \left[ \frac{F_n(\text{model})}{F_n(\text{obs.})} \right] \right|. \quad (1)$$

This procedure weights fainter lines equally with stronger lines, and is therefore more sensitive to the values of the input parameters of the model. Once a satisfactory best-fit is obtained ( $L1 = 0.051$ ), we adjust the abundances of the species which are unimportant in the thermal balance of the nebula, or for species for which only one or two emission lines are observed in the optical.

A detailed description of the photoionisation model fit is deferred until later, in order to also include the shocked zones of the nebular model.

## 5.2 The inner stellar wind bubble shock

In section 4.1 we estimated that the driving pressure of the shock driven by the X-ray bubble into the photoionised PNe material lies in the range  $\log P_s/k = 8.2 - 8.5 \text{ cm}^{-3}\text{K}$ . However, in the previous section, we found that the pre-shock pressure in the photoionised shell is only  $\log P_{PNe}/k = 7.4 \text{ cm}^{-3}\text{K}$ , and the total hydrogen particle density is  $n_H = 1400 \text{ cm}^{-3}$ . Adopting  $\log P_s/k = 8.4 \text{ cm}^{-3}\text{K}$ , we find that the resultant ram pressure can drive a  $40 \pm 5$  km/s (Mach number = 3) shock, which heats the immediate post-shock

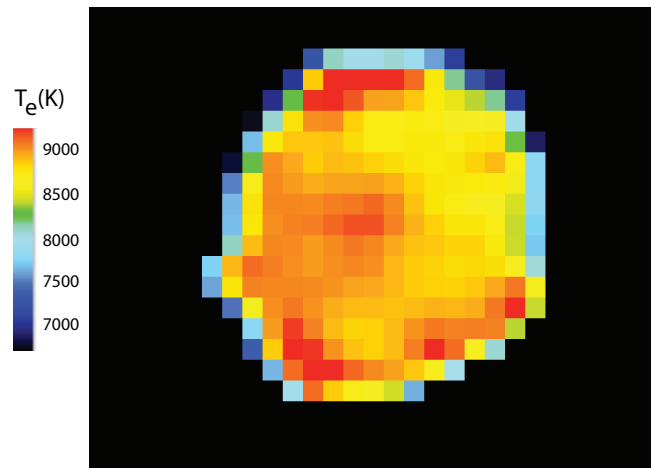


**Figure 5.** The [O III]  $\lambda\lambda 4363/4959$  line ratio map converted to mean temperature along the line of sight. The WiFeS image covers  $27 \times 22$  arc sec. Enhanced temperature associated with the inner shock can be clearly seen, as well as a radial temperature gradient followed by a steep decline at the boundary of the [O III] - emitting zone. This is in qualitative accord with the models which predict a temperature of  $T_e = 8840$  K in the inner shocked shell, an inner temperature of  $T_e = 8300$  K in the photoionised region rising to a peak of  $T_e = 9050$  K before declining to  $T_e = 8630$  K at the boundary of the [O III] - emitting zone.

gas to  $T_e = 30400$  K. As the gas cools, it is compressed, and reaches a computed electron density of  $n_e = 21800 \text{ cm}^{-3}$  where it is in equilibrium with the stellar radiation field. The computed equilibrium temperature is  $T_e = 8840$  K, somewhat higher than the equilibrium temperature in the inner photoionised shell ( $T_e \sim 8300$  K). From the model, the time taken for the shocked gas to reach photoionisation equilibrium is only  $\sim 10$  yr.

The  $H\beta$  flux from the shocked shell is only a small fraction of the total luminosity of the PNe. This fraction is roughly proportional to the mean age of the shocked shell. For an assumed age of 100 yr, it only accounts for  $\sim 1.0\%$  of the total  $H\beta$  flux. However, this shock contributes appreciably to the [O III] emission, since its [O III]  $\lambda 5007/H\beta$  ratio is 11.44. The shock contributes even more to the highest excitation lines. For example, the [Ne III]  $\lambda 3869/H\beta$  ratio in the shocked shell is 0.66, while in the nebula as a whole it is only 0.024. This shock contribution to the high excitation lines is a further reason why we derive a lower effective temperature for the central star than [Morisset & Georgiev \(2009\)](#).

The inner shock should manifest itself as a region of enhanced electron temperature. This is seen clearly in the WiFeS [O III]  $\lambda\lambda 4363/4959$  line ratio map; see Figure 5.

## 5.3 The outer shock in the AGB wind

The outer shock is a very slow shock proceeding into a medium with a low degree of ionisation. As such, it bears some resemblance to the Herbig-Haro shocks modelled by [Dopita & Sutherland \(2017, in press\)](#). Such shocks produce much enhanced [O I] and [N I] emission, and also enhanced [S II] emission. We model the shock with a velocity of 14 km/s, derived from the arguments presented in Section 4.3. The

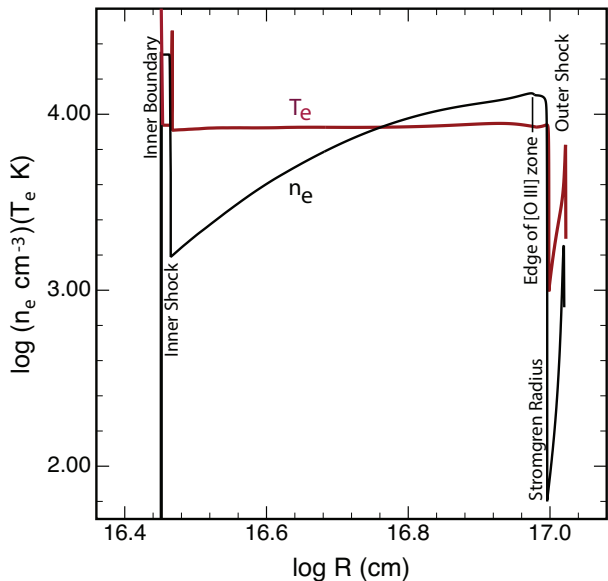


**Figure 6.** The run of electron temperature and density as a function of radius throughout the model. The major structural features are marked.

post-shock pressure is  $\log P/k = 8.4$ , which, with this shock velocity implies a pre-shock density of  $n_H = 10000 \text{ cm}^{-3}$ , at a fractional ionisation of a few percent.

The resulting shock is very feeble in its optical emission, accounting to only about 1.0% of the  $H\beta$  emission of the photoionised shell. However, the computed  $[\text{N I}] \lambda\lambda 5198, 5200/H\beta$  ratio is high, about 0.6, as is the  $[\text{O I}] \lambda 6300/H\beta$  ratio;  $\sim 1.5$ . As a consequence, the shock provides more than 50% of the total flux of these lines in the model. This accounts for the shortfall in  $[\text{N I}]$  and  $[\text{O I}]$  noted by the authors in the pure photoionisation model of [Morisset & Georgiev \(2009\)](#).

#### 5.4 Overall Structure of Model

The overall structure of the resulting model is shown in Figure 6, where we show the run of temperature and electron density as a function of radius. The inner shocked and photoionised shell is very thin with the post-shock temperature excursion appearing almost as a delta function. The steep rise in electron density though the main nebula is very evident, although the density variations are more subtle. The outer boundary of the  $[\text{O III}]$ -emitting zone is marked by small discontinuities in both temperature and density. The boundary of the Strömgen sphere is marked by a sharp drop in temperature and electron density. The outer shock produces a spike in both temperature and electron density.

In Table 4 we show the relative contributions of the inner and outer shocks to the total line fluxes of some key lines. These lines are the most sensitive to the presence of the shocks. The change in relative intensity for the model with and without shocks is at most a factor of two.

**Table 4.** The contribution of the inner and outer shocks to some strongly affected nebular line intensities as predicted by the model, all scaled to  $I(H\beta)=100$ .

Lambda (Å)	Ion	Nebula	Inner Shell	Outer Shock	Sum
3727,9	$[\text{O II}]$	171.2	15.0	4.2	168.3
3867	$[\text{Ne III}]$	2.4	65.0	0.0	2.9
4068	$[\text{S II}]$	1.9	0.04	2.8	1.9
4363	$[\text{O III}]$	0.87	7.2	0.0	0.91
4711	$[\text{Ar IV}]$	0.41	0.86	0.0	0.41
4861	$H\beta$	100	100	100	100
5007	$[\text{O III}]$	197.6	1114	0.0	202.9
5200	$[\text{N I}]$	0.24	0.0	21.3	0.45
6300	$[\text{O I}]$	1.72	0.0	60.0	2.28
Fractional		0.9824	0.0100	0.0076	1.000
Flux ( $H\beta = 1$ ):					

## 6 RESULTS OF THE MODEL

### 6.1 Emission Line Intensities

Our model provides predictions for a total of 154 emission lines in the optical spectrum of IC 418. For the permitted lines of heavy elements, the model only accounts for the recombination contribution to the line. As [Escalante et al. \(2012\)](#) demonstrated, the intensity of most of these lines are dominated by fluorescence. We have therefore used the ratio of fluorescence to recombination computed by these authors to correct our predictions for these lines. In Table 5 we present the list of modelled emission lines with their predicted fluxes relative to  $H\beta$ , the measured de-reddened line intensities and errors, as well as the de-reddened line intensities given by [Sharpee et al. \(2003\)](#) from their échelle observations. The lines marked with an asterisk (\*) have been corrected for the fluorescent process.

Overall the fit of the model with the observations is very good, with most of the predicted line strengths falling within  $\pm 20\%$  of the observed value. Strong lines which are poorly modelled are  $[\text{Ne III}]$  ( $\sim 25\%$  low) and  $[\text{S III}] \lambda 6312$  (overestimated by a factor of two – but this line is very sensitive to the electron temperature). The  $[\text{Fe II}]/[\text{Fe III}]$  ratios are poorly reproduced – but this ratio is very sensitive to the adopted charge-exchange reaction rates.

In Figure 7 we show the fit of the model versus the observations. Perfect agreement is represented by the central solid line, while the lines on each size represent a difference of  $\pm 20\%$  in the relative flux.

It is of interest to compare our measured line intensities with those given by [Sharpee et al. \(2003\)](#). These observations were made at much higher resolution than ours, and the integration times were much longer, which facilitates the detection of fainter lines. Against this, however, is the notorious difficulty of flux calibrating échelle data due to the strong variation in grating efficiency as one goes off-blaze in each order. Furthermore, the [Sharpee et al. \(2003\)](#) data covers only a portion of the nebula, which could cause problems associated with sampling the excitation structure of the nebula.

In Figure 8 we compare our own de-reddened data with the de-reddened fluxes given by [Sharpee et al. \(2003\)](#) for the same lines we used in the model fit. Perfect agreement is represented by the thick solid line, while the thinner lines on each size represent a difference of  $\pm 20\%$ . The agreement between these two independent data sets is remarkable, and

**Table 5.** A comparison of the observed line fluxes, the predictions of the model, and the line fluxes of Sharpee et al. (2003).

Wavelength (Å)	ID	Observed Flux (H $\beta$ =100)	Model	Sharpee03	Wavelength (Å)	ID	Observed Flux (H $\beta$ =100)	Model	Sharpee03
3613.642	He I	0.5110 ± 0.0242	0.4892	0.5577	4890.856	O II	0.0100 ± 0.0004	0.0030*	0.0137
3697.158	H I	1.4540 ± 0.1274	1.1670	1.6649	4921.931	He I	1.0721 ± 0.0186	1.2085	1.2186
3703.859	H I	1.7290 ± 0.3146	1.3710	1.9143	4931.227	[O III],[Fe III]	0.0321 ± 0.0007	0.0270	0.0294
3711.977	H I	2.0020 ± 0.0860	1.6340	2.2926	4958.911	[O III]	64.179 ± 1.0240	71.2760	72.7233
3721.750	H I,[S III]	3.0970 ± 0.1425	3.7458	3.3082	4987.210	[Fe III ]	0.0154 ± 0.0008	0.0140	0.0165
3726.032	[O II ]	126.580 ± 8.984	124.316	123.7908	4906.830	O II	0.0050 ± 0.0003	0.0045*	
3728.815	[O II ]	52.580 ± 10.901	51.6340	52.3426	4924.529	O II	0.0134 ± 0.0081	0.0070*	
3734.375	H I	2.7380 ± 0.1292	2.4490	3.0689	4994.360	N II	0.0310 ± 0.0008	0.0313*	0.0423
3750.158	H I	3.5430 ± 0.1603	3.0910	4.0585	5001.480	N II	0.0327 ± 0.0019	0.0366*	
3770.637	H I	4.4060 ± 0.1952	3.9970	4.0585	5006.843	[O III]	199.430 ± 5.017	206.0137	214.935
3777.134	He II	0.0053 ± 0.0010	0.0062	0.0050	5015.678	He I	2.2745 ± 0.0370	2.3269	2.3922
3797.904	H I	5.5240 ± 0.2487	5.3170	5.6643	5047.739	He I	0.1890 ± 0.0032	0.1685	0.1887
3835.391	H I	7.3140 ± 0.3354	7.3130	9.4921	5158.792	[Fe II]	0.0080 ± 0.0005	0.0041	0.0102
3864.431	O II	0.0067 ± 0.0033	0.0021*		5191.822	[Ar III]	0.0326 ± 0.0007	0.0400	0.0386
3868.764	Ne III ]	4.3060 ± 0.2226	3.0320	3.0916	5197.902	[N I ]	0.2818 ± 0.0036	0.2568	0.2011
3882.194	O II	0.0071 ± 0.0015	0.0100*	0.0063	5200.257	[N I ]	0.1547 ± 0.0022	0.3560	0.1173
3888.800	H I, He I	14.400 ± 1.071	19.6500	16.0294	5261.633	[Fe II]	0.0059 ± 0.0005	0.0117	0.0062
3933.663	Ca II	0.0042 ± 0.0005	0.0064		5270.403	[Fe III]	0.0231 ± 0.0006	0.0590	0.0151
3888.800	H I, He I	14.400 ± 1.0706	19.6500	16.0294	5273.364	[Fe II]	0.0030 ± 0.0004	0.0011	0.0018
3964.729	He I	0.8235 ± 0.0509	1.0545	0.9220	5452.080	N II	0.0019 ± 0.0005	0.0115*	0.0018
3967.471	[Ne III ]	1.3401 ± 0.1093	0.9133	0.9751	5462.590	N II	0.0042 ± 0.0004	0.0105*	0.0042
3970.079	H I	16.014 ± 0.5726	15.8730	16.8492	5478.086	N II	0.0025 ± 0.0002	0.0024*	0.003
4026.209	He I	1.8894 ± 0.0511	2.1130	2.0978	5480.060	N II	0.0053 ± 0.0003	0.0136*	0.0056
4035.080	N II	0.0023 ± 0.0005	0.0033	0.0071	5517.709	[Cl III]	0.1792 ± 0.0033	0.1995	0.1819
4041.310	N II	0.0059 ± 0.0014	0.0070	0.0121	5537.873	[Cl III ]	0.3651 ± 0.0070	0.4104	0.3560
4068.600	[S II],O II	2.3690 ± 0.0780	1.9391	1.8077	5577.339	[O I]	0.0308 ± 0.0010	0.0130	0.0263
4072.152	O II	0.0333 ± 0.0105	0.0359	0.0327*	5666.630	N II	0.0407 ± 0.0020	0.0384*	0.0414
4076.349	[S II]	0.8679 ± 0.0243	0.6228	0.7653	5676.020	N II	0.0191 ± 0.0094	0.0147*	0.0197
4087.153	O II	0.0057 ± 0.0009	0.0034	0.0045	5679.560	N II	0.0602 ± 0.0022	0.0661*	0.0674
4089.288	O II	0.0150 ± 0.0012	0.0150	0.0114	5686.210	N II	0.0112 ± 0.0007	0.0087*	0.0127
4095.644	O II	0.0203 ± 0.0083	0.0025	0.0042	5710.780	N II	0.0150 ± 0.0011	0.0140*	0.0136
4097.257	O II	0.0063 ± 0.0083	0.0096*	0.0115	5754.595	[N II]	2.7304 ± 0.0902	2.2960	2.7615
4101.742	H I	26.6525 ± 0.9271	25.8480	24.8041	5875.664	He I	12.4705 ± 0.4257	12.2260	13.6746
4104.723	O II	0.0243 ± 0.0106	0.0090*	0.0160	5927.810	N II	0.0160 ± 0.0009	0.0313*	0.0191
4110.786	O II	0.0111 ± 0.0019	0.0032*	0.0075	5931.790	N II	0.0215 ± 0.0015	0.0112*	0.0270
4120.835	He I	0.2022 ± 0.0069	0.1707	0.2062	5941.650	N II	0.0273 ± 0.0034	0.0142*	0.0315
4132.800	O II	0.0116 ± 0.0016	0.0099*	0.0083	5952.390	N II	0.0071 ± 0.0006	0.0074*	0.0052
4153.298	O II	0.0171 ± 0.0014	0.0129*	0.0184	6149.298	C II	0.0253 ± 0.0008	0.0150	0.0253
4267.140	C II	0.4896 ± 0.0115	0.3520	0.5712	6300.304	[O I]	2.8345 ± 0.0976	2.4365	2.1753
4275.551	O II	0.0052 ± 0.0003	0.0068	0.0065	6312.063	[S III]	0.8527 ± 0.0277	1.6550	0.8566
4277.894	O II	0.0006 ± 0.0002	0.0012	0.0033	6363.776	[O I]	0.9415 ± 0.0331	0.7793	0.7594
4294.700	O II	0.0030 ± 0.0005	0.0029	0.0059	6527.231	[N II]	0.0290 ± 0.0015	0.0280	0.0285
4303.823	O II	0.0078 ± 0.0007	0.0007	0.0066	6548.052	[N II]	49.2466 ± 1.5995	52.3040	53.6007
4307.232	O II	0.0129 ± 0.0010	0.0013	0.0119	6562.819	H I	283.3268 ± 9.7787	287.0080	312.043
4315.360	O II	0.0020 ± 0.0005	0.0006		6578.053	He I,C II	0.5215 ± 0.0243	0.5316	0.5374
4332.694	O II	0.0018 ± 0.0008	0.0021*		6583.454	[N II]	147.2072 ± 5.0507	153.8852	162.9287
4340.471	H I	48.0351 ± 1.0194	46.7602	44.8053	6678.152	He I	3.2936 ± 0.1118	3.4798	3.8721
4363.209	[O III]	0.7882 ± 0.0194	0.9280	0.9353	6716.440	[S II]	2.2171 ± 0.0692	2.1834	2.0831
4387.929	He I	0.4925 ± 0.0117	0.5603	0.5462	6730.816	[S II]	4.5866 ± 0.1622	4.2908	4.4215
4437.553	He I	0.0716 ± 0.0019	0.0696	0.0792	7135.792	[Ar III]	7.0589 ± 0.2750	7.4260	8.2608
4471.502	He I	3.9804 ± 0.0924	4.1424	4.4921	7231.327	C II	0.1939 ± 0.0100	0.4112*	0.1692
4491.222	O II	0.0119 ± 0.0008	0.0021	0.0125	7236.416	C II	0.5055 ± 0.0230	0.4915*	0.4673
4566.837	Mg I]	0.5226 ± 0.0124	0.5220	0.4291	7281.351	He I	0.7404 ± 0.0221	0.6080	0.7911
4601.478	N II	0.0232 ± 0.0009	0.0209*	0.0263	7291.469	Ca II	0.0149 ± 0.0010	0.0150	0.0123
4607.100	N II	0.0235 ± 0.0008	0.0206*	0.0257	7318.923	[O II]	3.7000 ± 0.3500	3.5080	3.6886
4613.868	N II	0.0159 ± 0.0008	0.0131*	0.0182	7319.989	[O II]	10.7196 ± 0.8900	10.4340	10.0586
4621.390	N II	0.0211 ± 0.0008	0.0262*	0.0264	7329.665	[O II]	6.5190 ± 0.3530	5.8160	5.8617
4630.540	N II	0.0683 ± 0.0019	0.0737*	0.0805	7330.735	[O II]	5.7000 ± 0.3300	5.5320	5.6377
4643.086	N II	0.0298 ± 0.0012	0.0281*	0.0344	7377.829	[Ni II]	0.0042 ± 0.0023	0.0042	0.0049
4658.051	[Fe III]	0.0035 ± 0.0020	0.0689	0.0274	7751.109	[Ar III]	1.8159 ± 0.0788	1.7879	2.1967
4667.010	[Fe III]	0.0035 ± 0.0005	0.0038	0.0028	7771.944	O I	0.0282 ± 0.0012	0.0162	0.0352
4699.218	O II	0.0097 ± 0.0097	0.0183*	0.0133	7774.166	O I	0.0195 ± 0.0009	0.0162	0.0215
4701.535	[Fe III]	0.0162 ± 0.0006	0.0320		7775.388	O I	0.0115 ± 0.0005	0.0162	0.0130
4705.346	O II	0.0147 ± 0.0005	0.0214	0.0183	8433.661	[Cl III]	0.0095 ± 0.0014	0.0110	0.0062
4713.171	He I	0.5881 ± 0.0144	0.4445	0.6098	8437.955	H I	0.4057 ± 0.0153	0.3370	0.4345
4733.906	[Fe III]	0.0067 ± 0.0005	0.0140	0.0048	8467.254	H I	0.4645 ± 0.0210	0.3940	0.5050
4740.123	[Ar IV]	0.0040 ± 0.0005	0.0044	0.0036	8480.859	[Cl III]	0.0113 ± 0.0007	0.0110	0.0108
4754.687	[Fe III]	0.0080 ± 0.0005	0.0130	0.0047	8502.483	H I	0.5459 ± 0.0202	0.4660	0.5983
4769.431	[Fe III]	0.0039 ± 0.0004	0.0110	0.0062	8545.383	H I	0.6407 ± 0.0241	0.5600	0.6807
4779.720	N II	0.0151 ± 0.0006	0.0305*	0.0179	8616.950	[Fe II]	0.0096 ± 0.0007	0.0105	0.0094
4788.130	N II	0.0166 ± 0.0007	0.0185*	0.0195	8578.697	[Cl II]	0.3165 ± 0.0119	0.1927	0.2844
4803.290	N II	0.0176 ± 0.0009	0.0102*	0.0261	8598.392	H I	0.7708 ± 0.0284	0.6840	0.8362
4810.299	N II	0.0026 ± 0.0006	0.0035*	0.004	8665.018	H I	0.9290 ± 0.0349	0.8500	0.9501
4814.544	[Fe II]	0.0040 ± 0.0005	0.0013	0.008	8727.126	[C I]	0.0373 ± 0.0016	0.0393	0.0334
4861.333	H I	100.000 ± 0.480	100.000	100.000	8750.472	H I	1.1829 ± 0.0437	1.0780	1.3112
4880.996	[Fe III]	0.0231 ± 0.0012	0.0760	0.0154	8829.391	[S III]	0.0059 ± 0.0004	0.0110	0.0048
4889.623	[Fe II]	0.0046 ± 0.0005	0.0011		8862.783	H I	1.5432 ± 0.0588	1.3990	1.6217

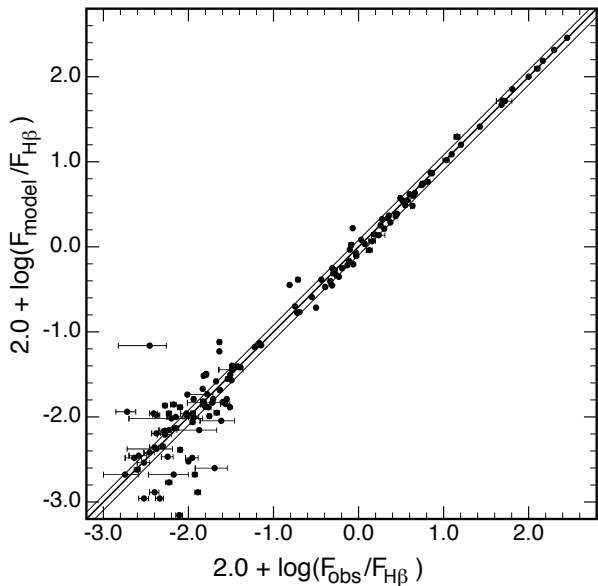


**Figure 7.** The fit of the model versus the (de-reddened) observations of IC 418. The dynamic range of the fitted intensities is  $\sim 10^5$ . Apart from some faint recombination lines, the quality of the fit for individual lines is generally better than  $\pm 20\%$ .

bears testament to the both the quality of the observations and data reduction procedures. Furthermore, it is clear that the observing strategy of [Sharpee et al. \(2003\)](#) enabled them to obtain a good approximation to the integral spectrum of the nebula.

## 6.2 The Nebular Continuum

The fit of the measured (de-reddened) nebular continuum (black points) with the theoretical (continuum + emission line) spectrum of the PNe (blue line) is shown in [Figure 9](#). It is clear that the theoretical continuum provides a good description of the observations except in the region  $\lambda\lambda 3650 - 4050\text{\AA}$ . This difference is due to either mis-measurement of the underlying continuum in the presence of many faint overlapping lines – many lines are fit with a fixed width in this wavelength region – or else scattering of the stellar UV by dust in and around the nebula. The size of both the Paschen and Balmer jumps are well simulated, as is the overall slope of the continuum, indicating that the mean nebular temperature characterising the model is close to that prevailing in the nebula itself.

## 6.3 Chemical Abundances

The abundances derived in the model are listed in [Table 6](#). Here we give separately the measured gas phase abundances, and the implied total abundances using the dust depletion pattern for the local interstellar medium from [Jenkins \(2009\)](#) for a base  $\log Fe/H$  depletion of  $-2.25$ . Clearly, we do not expect the dust in IC 418 to share this depletion pattern, so the total (Gas + Dust) abundances given in the table should

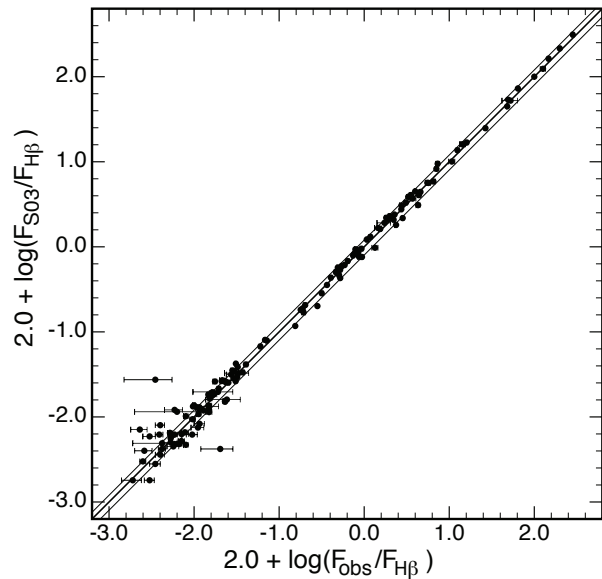


**Figure 8.** The fit of the observed (de-reddened) line fluxes versus the de-reddened observations by [Sharpee et al. \(2003\)](#) (S03) of these same lines in IC 418. The scatter between these two data sets is generally less than  $\pm 20\%$  over the full dynamic range.

be treated as indicative only. [Table 6](#) also compares our results with the gas phase abundances derived by [Morisset & Georgiev \(2009\)](#). This paper also presents the comparison with earlier work. Considering that we are using an independent data set, different analysis techniques, and different modelling codes, we find that the mutual agreement for the important coolants is very good, generally better than 0.1 dex.

As described above, we have used the Nebular Empirical Abundance Tool (NEAT; [Wesson et al. \(2012\)](#)) to derive the electron temperature and density from the low and medium-ionization zones. In [Table 6](#), we also present the elemental abundances of nitrogen, oxygen, neon, argon, sulfur, and chlorine that determined from collisionally excited lines (CELs) and those of hydrogen, helium, carbon derived from optical recombination lines (ORLs). The ionization correction factors of [Delgado-Inglada et al. \(2014\)](#) were used to correct for unseen ions. The chemical abundances are found to be in agreement with that of [Delgado-Inglada et al. \(2015\)](#) and [Pottasch et al. \(2004\)](#). However, in general, the chemical abundances are generally systematically lower than those derived by the detailed modelling presented here, and those derived in a similar manner by [Morisset & Georgiev \(2009\)](#). This illustrates once again the perennial problem of differences between  $T_e$ -derived abundances, and those delivered by detailed photoionisation modelling. Abundances delivered by  $T_e$ +ICF calibration are systematically lower than those used in the photoionisation models. This is mainly caused by regions of higher than average temperature over-weighting temperature-sensitive lines such as [O III]  $\lambda 4363$ . The ICFs do not seem to be playing a major role, since the computed ICFs agree in broad agreement with the photoionisation model (for OI:OII:OIII we have the ratios

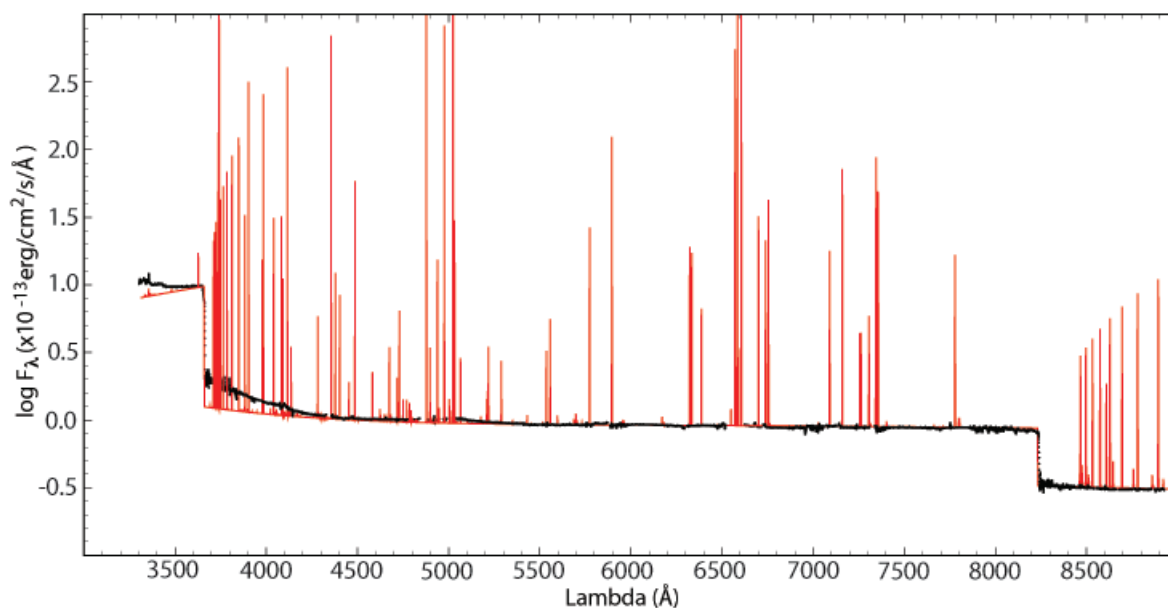


**Figure 9.** The fit of the model spectrum (in red) with the (de-reddened) observations of the continuum in IC 418 (in black). The fitted emission lines have been removed from this spectrum. The rise in the apparent continuum below 4000Å is largely due to the mis-measurement of the underlying continuum in the presence of many faint overlapping lines. There may also be scattered light resulting from dust scattering of the stellar UV continuum.

0.024:0.490:0.486 from the ICFs given by NEAT, while the ionic column densities from the model are in the ratio 0.018:0.496:0.486. At least part of the disagreement between the two techniques is due to real temperature gradients we have demonstrated to exist in IC 418 (c.f. Figure 5). These large-scale temperature gradients play a role analogous to the smaller-scale temperature fluctuations first introduced by Peimbert (1967) and used by very many others since, e.g. Esteban et al. (2002); García-Rojas & Esteban (2007); Peña-Guerrero et al. (2012). In particular, Kingdon & Ferland (1995) has attempted to reproduce temperature fluctuations in the context of temperature variations produced in detailed phototisation models.

The fluorescent corrections given by Escalante et al. (2012) work rather well to remove the abundance discrepancy, which is often inferred to exist in other PNe, between the permitted and the forbidden lines. In Figure 10 we show the comparison of the model predictions for the forbidden lines (filled circles) and the fluorescent - corrected “recombination” lines of N II and O II (open circles). The error bars refer to the line measurement errors only.

#### 6.4 Comparison with the UV and IR spectrum

Although we have not specifically modelled the UV and IR spectrum of IC 418, nonetheless it is of interest to see how well the model performs in reproducing the de-reddened UV and IR line intensities given by Pottasch et al. (2004) and by Liu et al. (2001), who used the LWS on the ISO observatory to measure the longer wavelength (43-198 $\mu$ m) lines. The comparison between the model and these observations is given in Table 7. Overall, for the IR lines, the fit is satisfactory – with the exception of [O I] and [C II] lines the

**Table 6.** The measured gas phase and implied total (Gas+ Dust) abundances. The gas phase abundances may be compared with the Morisset & Georgiev (2009) abundances (MG09), and with the abundances derived from the NEAT code.

Element	12 + log(X/H)			
	Gas Phase	Total	MG09	NEAT
H	12.00	12.00	12.00	12.00
He	11.04	11.04	11.08	10.90
C	8.71	8.92	8.90	8.74
N	7.98	8.08	8.00	7.65
O	8.62	8.86	8.60	8.34
Ne	8.14	8.14	8.00	7.50
Mg	7.04	8.32	7.05	—
Si	6.84	7.50	7.10	—
S	6.89	6.89	6.65	6.28
Cl	4.89	5.70	5.00	4.95
Ar	6.08	6.08	6.20	6.23
Ca	3.84	6.99	—	—
Fe	4.97	7.22	4.60	—
Ni	4.02	6.46	—	—

L1-norm is 0.12. For the UV lines (with their larger and more uncertain reddening corrections) the L1-norm is 0.17. All the oxygen lines fit the observations very closely.

As Liu et al. (2001) point out, IC 418 is blessed with an exceptionally strong photo-dissociation region (PDR) which provides a large contribution to the observed intensity of the [O I] and [C II] lines. However, since the MAPPINGS code does not include a molecular formation/destruction chemical matrix, but only deals with atomic phases, we cannot model the temperature, density and molecular / ion balance in PDRs with any accuracy. Any prediction of the [O I] and

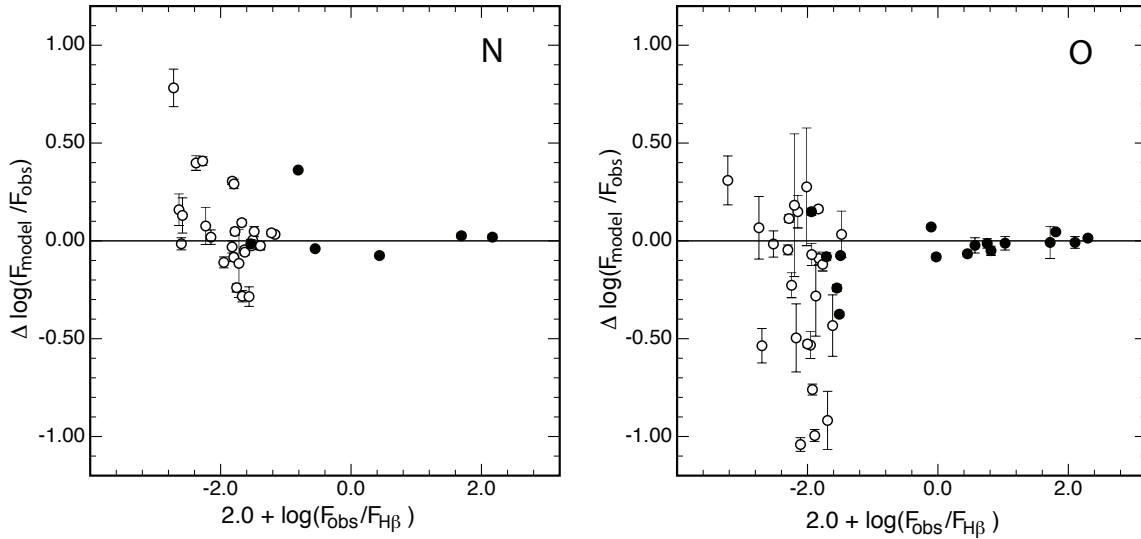


**Figure 10.** A comparison of the IC 418 model fit for the fluorescence - corrected permitted lines of N II and O II (open circles) and the corresponding fit for the forbidden lines of any ionisation stage (filled circles). The effect of the fluorescence corrections given by Escalante et al. (2012) are to remove the abundance discrepancy between permitted and forbidden lines that would otherwise have been present.

[C II] lines would therefore be completely unreliable. This is clear from Table 7. All we can do with reasonable accuracy is to compute the dust temperature distribution in these regions.

The  $35.81\mu\text{m}$  [Si II] line is the only line of this element observed, and this has been used to determine the Si abundance shown in Table 7, although this line might be dominated by the contribution of emission from the PDR. The Mg abundance was obtained from only one line in the optical spectrum, so it is pleasing to see how well the modelled Mg II  $2798\text{\AA}$  line matches the observations. The carbon lines provide a useful further constraint on the abundance estimated from the [C I]  $\lambda 8727$  line, and from the four C II permitted lines which are observed in the optical.

### 6.5 Surface Brightness Distribution

As described above, the radiation pressure induces a steep density gradient in the ionised plasma, which leads to an increase in the projected surface brightness with radius. In addition, the inner shock contributes appreciably to the  $H\alpha$  surface brightness. On the basis of our idealised spherical model, we have computed the surface brightness as a function of radius. This is shown in Figure 11.

This surface brightness distribution can be compared with that shown by Morisset & Georgiev (2009). The inner shock appears sharper here because it is represented by a smooth spherical shock, rather than the more filamentary structure seen in the HST data.

## 7 DISCUSSION & CONCLUSIONS

We have presented a physical model for IC 418 which provides a good description of the emission line spectrum, while at the same time matching the density sensitive line ratios,

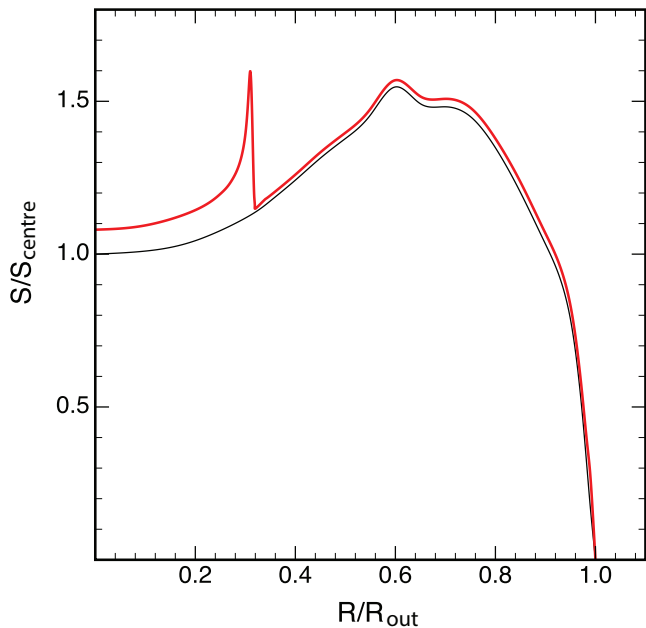
**Table 7.** The comparison of the model with UV and IR lines observed by Pottasch et al. (2004) and Liu et al. (2001) in IC 418. Line fluxes are relative to  $H\beta = 100$ .

Lambda ( $\text{\AA}$ )	Ion	Flux	Model
1663	O III	< 0.7	0.71
1750	N III	0.58	0.87
1909	C III	27.59	49.3
2325	C II	81.2	44.5
2471	[O II]	19.2	19.8
2798	Mg II	16.3	21.57

Lambda( $\mu\text{m}$ )	Ion	Flux	Model
2.625	H I	4.7	4.68
4.052	H I	8.6	8.21
7.46	H I	2.7	2.61
8.99	[Ar III]	7.3	7.39
10.51	[S IV]	1.3	2.05
12.81	[Ne II]	53.1	82.7
15.55	[Ne III]	9.5	4.23
18.71	[S III]	15.2	24.4
33.47	[S III]	2.6	4.31
34.81	[Si II]	0.9	0.90
51.81	[O III]	14.7	14.6
57.34	[N III]	3.2	3.2
63.10	[O I]	10.1	0.34
88.36	[O III]	2.4	1.95
121.8	[N II]	0.16	0.21
145.6	[O I]	0.10	0.24
157.7	[C II]	0.99	0.37

the inferred absolute  $H\beta$  flux and the observed angular diameter of the nebula. From the photoionisation model we estimate a distance of  $1.0 \pm 0.1$  kpc, slightly less than the value usually adopted. This result is due to the strong com-



**Figure 11.** The computed brightness distribution for IC 418. The black curve is for the photoionised nebula only, while the red curve shows how this is modified by the presence of the two shocks.

petition of dust for the ionising photons in a nebula in which radiation pressure exceeds the static gas pressure. The absorption of the UV radiation field leads to steeply increasing pressure and density with nebular radius.

We estimate the stellar parameters to be  $\log T_{eff} = 4.525\text{K}$ ,  $\log L_*/L_\odot = 4.029$  and  $\log g = 3.5$ . From the hydrogen-burning Vassiliadis & Wood (1994) evolutionary tracks, we find that this corresponds to an initial stellar mass of  $\sim 2.8M_\odot$ . This derived mass of the parent star is consistent with the mass range ( $1.5 - 3.0M_\odot$ ) reported by Delgado-Inglada et al. (2015) for the PNe which give rise to carbon-rich dust (see the introduction). Interpolating the hydrogen-burning  $Z = 0.016$  Vassiliadis & Wood (1994) evolutionary tracks, we also find that the star has had only  $\sim 180\text{yr}$  since it passed through an effective temperature of  $\log T_{eff} = 4.0$ , which can be taken effectively as the time since the nebula first became ionised. Very similar results are obtained if we use the more recent models of Miller Bertolami (2016). For  $Z = 0.01$ , the precursor would have had an initial mass of  $2.5M_\odot$ , while for  $Z = 0.02$ , the estimated initial mass rises to  $3.0M_\odot$ . In both cases the transition time from an effective temperature  $\log T_{eff} = 3.8\text{K}$  is  $\sim 100\text{yr}$ .

Integrating the density throughout the nebula in the model, we find that the total mass inside the ionised nebula out to where hydrogen is less than 1% ionised is  $4.8 \times 10^{-2}M_\odot$ . Since the nebula is composed of the gas ejected during the last gasp of the AGB stellar evolution, this mass represents the integrated mass loss over the last 2350 yr, using the outer radius of  $1.0 \times 10^{17}\text{cm}$ , and taking the velocity of the AGB wind to be  $13.2\text{km/s}$  from Taylor & Pottasch (1987). From the previous paragraph, we can infer that the time that the central star actually spent on the AGB during this period was only 2270 yr, which implies a mean AGB mass-loss rate of  $2.1 \times 10^{-5}M_\odot/\text{yr}$ . This is entirely consistent

with recent mass-loss rates inferred directly from the 1612 MHz circum-stellar OH maser emission for a large sample of AGB stars by Goldman et al. (2017).

The age of the nebula can also be inferred from the properties of the central mass-loss bubble. Currently, according to the model, the shock in the nebular gas is propagating at  $\sim 40\text{km/s}$ . The radius of the shocked [O III] - bright bubble is  $\sim 0.01\text{pc}$ . Using the theory of such bubbles (Dyson & de Vries 1972; Weaver et al. 1977), we derive an age of 150 yr for the mass-loss bubble, which agrees well with the age inferred above from stellar evolutionary considerations (100–180 yr).

Based upon the stellar wind velocity derived from the X-ray temperature of the hot inner bubble ( $v_w \sim 500\text{km/s}$ ), and the pressure in the hot bubble equated to the ram pressure driving the mass-loss bubble shock in the nebular gas ( $\log P_s/k = 8.4\text{cm}^{-3}\text{K}$ ), and assuming that the free wind region from the central star is terminated at 60% of the radius of the inner mass-loss bubble, we infer that the current mass loss rate from the central star is  $\dot{M} \sim 5 \times 10^{-8}M_\odot\text{yr}^{-1}$ , which agrees well with that obtained by Morisset & Georgiev (2009) on the basis of the absorption line profiles of the central star ( $\dot{M} = 3.8 \times 10^{-8}M_\odot\text{yr}^{-1}$ ).

The ionised structure appears to be very young; 150–200 yr. This presents something of a problem, since the sound-crossing timescale of the current ionised structure is  $\sim 2000\text{yr}$ , yet the internal density distribution has already been set up as a radiation-dominated nebula. This would seem to indicate that the radiation-pressure dominated profile is actually set up during the transition from the tip of the AGB to the point where the central star started to produce ionising photons. According to the Miller Bertolami (2016) models cited above, for  $Z = 0.01$ , this transition time is  $\sim 1600\text{yr}$ , while for  $Z = 0.02$ , it is  $\sim 1200\text{yr}$ . Both of these are comparable with the inferred sound crossing timescale.

In conclusion, we have obtained a high-quality integral field spectrum of IC 418, and have built a self-consistent model for the nebula which includes both the effects of the inner mass-loss bubble, and the outer shock in the AGB wind. Consequently we have been able to derive reliable abundances for 14 elements, which agree well with the earlier careful modelling by Morisset & Georgiev (2009). In addition, our measured line fluxes relative to  $\text{H}\beta$  agree very closely, typically within 10%, with those of Sharpee et al. (2003), despite the differences in the instruments used, the area over which the spectrum is integrated and the differences in both the reduction and calibration procedures. IC 418 is both dusty and carbon-rich, and its central star appears to have been a fairly massive carbon star with an initial mass in the range  $2.5 - 3.0M_\odot$  and an AGB mass-loss rate of  $2.1 \times 10^{-5}M_\odot/\text{yr}$  before it made its excursion across the HR Diagram to become a PNe central star with mass-loss rate of  $\dot{M} \sim 4 \times 10^{-8}M_\odot/\text{yr}$ .

## ACKNOWLEDGEMENTS

The authors wish to thank the referee, Christophe Morisset for his physical insights, and his careful and constructive critique, which has appreciable improved the paper. M.D. and R.S. acknowledge the support of the Australian Research Council (ARC) through Discovery project DP130103925.

## REFERENCES

- Acker A., Marcout J., Ochsenbein F., Stenholm B., Tylenda R., Schohn C., 1992, *The Strasbourg-ESO Catalogue of Galactic Planetary Nebulae*. Parts I, II. European Southern Observatory, Garching (Germany), 1992, 1047 p., ISBN 3-923524-41-2,
- Ali A., Amer M. A., Dopita M. A., Vogt F. P. A., Basurah H. M., 2015, *A&A*, **583**, A83
- Ali A., Dopita M. A., Basurah H. M., Amer M. A., Alsulami R., Alruhaili A., 2016, *MNRAS*, **462**, 1393
- Axford W. I., 1964, *ApJ*, **140**, 112
- Basurah H. M., Ali A., Dopita M. A., Alsulami R., Amer M. A., Alruhaili A., 2016, *MNRAS*,
- Capriotti E. R., Daub C. T., 1960, *ApJ*, **132**, 677
- Carrasco L., Serrano A., Costero R., 1983, *Rev. Mex. Astron. Astrofis.*, **8**, 187
- Childress M. J., Vogt F. P. A., Nielsen J., Sharp R. G., 2014, *Ap&SS*, **349**, 617
- Danehkar A., 2015, *ApJ*, **815**, 35
- Danehkar A., Parker Q. A., 2015, *MNRAS*, **449**, L56
- Danehkar A., Parker Q. A., Steffen W., 2016, *AJ*, **151**, 38
- Davies R. L., et al., 2016, *ApJ*, **824**, 50
- Delgado-Inglada G., Morisset C., Stasińska G., 2014, in *Revista Mexicana de Astronomía y Astrofísica Conference Series*. pp 17–17
- Delgado-Inglada G., Rodríguez M., Peimbert M., Stasińska G., Morisset C., 2015, *MNRAS*, **449**, 1797
- Díaz-Luis J. J., García-Hernández D. A., Kameswara Rao N., Manchado A., Cataldo F., 2015, *A&A*, **573**, A97
- Dopita M. A., Sutherland R. S., 2000, *ApJ*, **539**, 742
- Dopita M. A., Groves B. A., Sutherland R. S., Binette L., Cecil G., 2002, *ApJ*, **572**, 753
- Dopita M. A., Groves B. A., Sutherland R. S., Kewley L. J., 2003, *ApJ*, **583**, 727
- Dopita M. A., et al., 2005, *ApJ*, **619**, 755
- Dopita M. A., et al., 2006, *ApJ*, **639**, 788
- Dopita M., Hart J., McGregor P., Oates P., Bloxham G., Jones D., 2007, *Ap&SS*, **310**, 255
- Dopita M., et al., 2010, *Ap&SS*, **327**, 245
- Dopita M. A., Sutherland R. S., Nicholls D. C., Kewley L. J., Vogt F. P. A., 2013, *ApJS*, **208**, 10
- Dyson J. E., de Vries J., 1972, *A&A*, **20**, 223
- Escalante V., Morisset C., Georgiev L., 2012, *MNRAS*, **426**, 2318
- Esteban C., Peimbert M., Torres-Peimbert S., Rodríguez M., 2002, *ApJ*, **581**, 241
- Frieman E. A., 1954, *ApJ*, **120**, 18
- García-Rojas J., Esteban C., 2007, *ApJ*, **670**, 457
- García-Segura G., Franco J., 1996, *ApJ*, **469**, 171
- Goldman S. R., et al., 2017, *MNRAS*, **465**, 403
- Grevesse N., Asplund M., Sauval A. J., Scott P., 2010, *Ap&SS*, **328**, 179
- Groves B., Dopita M. A., Williams R. E., Hua C.-T., 2002, *Publ. Astron. Soc. Australia*, **19**, 425
- Guerrero M. A., Toalá J. A., Medina J. J., Luridiana V., Miranda L. F., Riera A., Velázquez P. F., 2013, *A&A*, **557**, A121
- Guzman-Ramirez L., Rizzo J. R., Zijlstra A. A., García-Miró C., Morisset C., Gray M. D., 2016, *MNRAS*, **460**, L35
- Guzmán L., Loinard L., Gómez Y., Morisset C., 2009, *AJ*, **138**, 46
- Hillier D. J., Miller D. L., 1998, *ApJ*, **496**, 407
- Hoare M. G., 1990, *MNRAS*, **244**, 193
- Jenkins E. B., 2009, *ApJ*, **700**, 1299
- Kahn F. D., 1954, *Bull. Astron. Inst. Netherlands*, **12**, 187
- Kahn F. D., 1958, *Reviews of Modern Physics*, **30**, 1058
- Kaler J. B., 1973, in *Remy-Battiau L., Vreux J. M., Menzel D. H., eds, Liege International Astrophysical Colloquia Vol. 18, Liege International Astrophysical Colloquia*. pp 33–47
- Kingdon J. B., Ferland G. J., 1995, *ApJ*, **450**, 691
- Kramida, A., Ralchenko, Yu., Reader, J. & The NIST ASD Team, 2012, *NIST Atomic Spectra Database (ver. 5.0)*, National Institute of Standards and Technology, Gaithersburg, MD.
- Liu X.-W., et al., 2001, *MNRAS*, **323**, 343
- Lodders K., Palme H., Gail H.-P., 2009, *Landolt Börnstein*, p. 44
- Marten H., Schoenberner D., 1991, *A&A*, **248**, 590
- Mathis J. S., Rimpl W., Nordsieck K. H., 1977, *ApJ*, **217**, 425
- Meixner M., Skinner C. J., Keto E., Zijlstra A., Hoare M. G., Arens J. F., Jernigan J. G., 1996, *A&A*, **313**, 234
- Mendis D. A., 1969, *MNRAS*, **142**, 241
- Miller Bertolami M. M., 2016, *A&A*, **588**, A25
- Mizuta A., Takabe H., Kane J. O., Remington B. A., Ryutov D. D., Pound M. W., 2005, *Ap&SS*, **298**, 197
- Monreal-Ibero A., Roth M. M., Schönberner D., Steffen M., Böhm P., 2005, *ApJ*, **628**, L139
- Morisset C., Georgiev L., 2009, *A&A*, **507**, 1517
- Morisset C., Szczerba R., Anibal García-Hernández D., García-Lario P., 2012, in *IAU Symposium*. pp 452–453, [arXiv:1110.2328](https://arxiv.org/abs/1110.2328), doi:10.1017/S174392131201188X
- Nicholls D. C., Sutherland R. S., Dopita M. A., Kewley L. J., Groves B. A., 2017, *MNRAS*, **466**, 4403
- Nieva M.-F., Przybilla N., 2012, *A&A*, **539**, A143
- O’Dell C. R., 1962, *ApJ*, **135**, 371
- Omont A., et al., 1995, *ApJ*, **454**, 819
- Otsuka M., Kemper F., Cami J., Peeters E., Bernard-Salas J., 2014, *MNRAS*, **437**, 2577
- Peña-Guerrero M. A., Peimbert A., Peimbert M., Ruiz M. T., 2012, *ApJ*, **746**, 115
- Peimbert M., 1967, *ApJ*, **150**, 825
- Perek L., 1971, *Bulletin of the Astronomical Institutes of Czechoslovakia*, **22**, 103
- Phillips J. P., 2003, *MNRAS*, **344**, 501
- Pottasch S. R., Bernard-Salas J., 2010, *A&A*, **517**, A95
- Pottasch S. R., Wesselius P. R., Wu C.-C., van Duinen R. J., 1977, *A&A*, **54**, 435
- Pottasch S. R., Bernard-Salas J., Beintema D. A., Feibelman W. A., 2004, *A&A*, **423**, 593
- Prinja R. K., Massa D. L., Urbaneja M. A., Kudritzki R.-P., 2012, *MNRAS*, **422**, 3142
- Ramos-Larios G., Vázquez R., Guerrero M. A., Olgún L., Marquez-Lugo R. A., Bravo-Alfaro H., 2012, *MNRAS*, **423**, 3753
- Ruiz N., Chu Y.-H., Gruendl R. A., Guerrero M. A., Jacob R., Schönberner D., Steffen M., 2013, *ApJ*, **767**, 35
- Sahai R., Morris M. R., Villar G. G., 2011, *AJ*, **141**, 134
- Schmidt-Voigt M., Koeppen J., 1987, *A&A*, **174**, 211
- Schmidt-Voigt M., Koppen J., 1987, *A&A*, **174**, 223
- Scott P., et al., 2015a, *A&A*, **573**, A25
- Scott P., Asplund M., Grevesse N., Bergemann M., Sauval A. J., 2015b, *A&A*, **573**, A26
- Sharpee B., Williams R., Baldwin J. A., van Hoof P. A. M., 2003, *ApJS*, **149**, 157
- Sharpee B., Baldwin J. A., Williams R., 2004, *ApJ*, **615**, 323
- Spitzer Jr. L., 1954, *ApJ*, **120**, 1
- Steffen M., Hubrig S., Todt H., Schöller M., Hamann W.-R., Sandin C., Schönberner D., 2014, *A&A*, **570**, A88
- Taylor A. R., Pottasch S. R., 1987, *A&A*, **176**, L5
- Tsamis Y. G., Walsh J. R., Pequignot D., Barlow M. J., Liu X.-W., Danziger I. J., 2007, *The Messenger*, **127**, 53
- Vassiliadis E., Wood P. R., 1993, *ApJ*, **413**, 641
- Vassiliadis E., Wood P. R., 1994, *ApJS*, **92**, 125
- Weaver R., McCray R., Castor J., Shapiro P., Moore R., 1977, *ApJ*, **218**, 377
- Wesson R., Stock D. J., Scicluna P., 2012, *MNRAS*, **422**, 3516
- Whalen D. J., Norman M. L., 2008, *ApJ*, **672**, 287
- Williams R. J. R., 1999, *MNRAS*, **310**, 789